IMAGING CARBON MONOXIDE EMISSION IN THE STARBURST GALAXY NGC 6000

SERGIO MARTÍN[1,2], MATTHEW R. GEORGE[2,3], DAVID J. WILNER[2], AND DANIEL ESPADA[2,4]

[1] European Southern Observatory, Alonso de Córdova 3107, Vitacura, Casilla 19001, Santiago 19, Chile; smartin@eso.org
[2] Harvard-Smithsonian Center for Astrophysics, 60 Garden Street, Cambridge, MA 02138, USA
[3] Department of Astronomy, University of California, Berkeley, CA 94720, USA
[4] Instituto de Astrofísica de Andalucía, CSIC, Granada, Spain

ABSTRACT

We present measurements of carbon monoxide emission in the central region of the nearby starburst NGC 6000 taken with the Submillimeter Array. The $J = 2$–1 transition of ^{12}CO, ^{13}CO, and C^{18}O were imaged at a resolution of $\sim 3'' \times 2''$ (450×300 pc). We accurately determine the dynamical center of NGC 6000 at $\alpha_{J2000.0} = 15^h49^m49^s.5$ and $\delta_{J2000.0} = -29°23'13''$ which agrees with the peak of molecular emission position. The observed CO dynamics could be explained in the context of the presence of a bar potential affecting the molecular material, likely responsible for the strong nuclear concentration where more than 85% of the gas is located. We detect a kinematically detached component of dense molecular gas at relatively high velocity which might be fueling the star formation. A total nuclear dynamical mass of $7 \times 10^9 \, M_\odot$ is derived and a total mass of gas of $4.6 \times 10^8 \, M_\odot$, yielding a $M_{\rm gas}/M_{\rm dyn} \sim 6\%$, similar to other previously studied barred galaxies with central starbursts. We determined the mass of molecular gas with the optically thin isotopologue C^{18}O and we estimate a CO-to-H$_2$ conversion factor $X_{\rm CO} = 0.4 \times 10^{20} \, {\rm cm}^{-2} ({\rm K \, km \, s}^{-1})^{-1}$ in agreement with that determined in other starburst galaxies.

Key words: galaxies: fundamental parameters – galaxies: ISM – galaxies: kinematics and dynamics – galaxies: nuclei – galaxies: starburst – radio lines: galaxies

1. INTRODUCTION

The relation between the morphology and kinematics of the gas in the inner region of galaxies and the connection to its nuclear activity is not completely understood. Nuclear regions are often obscured by dust at optical wavelengths but can be viewed in continuum infrared dust emission as well as molecular line emission. CO can be used as a tracer of molecular gas, and its rotational transitions are observed at millimeter and submillimeter wavelengths. Observations of the morphology and kinematics of the molecular gas content in the central regions of spirals can provide insight into the dynamical processes occurring there (e.g., Jogee et al. 2005; Pérez-Ramírez et al. 2000). Studies indicate that instabilities in bars and dissipation of gas clouds remove angular momentum from material orbiting the galactic center, driving gas and dust inward to fuel star formation (e.g., Pfenniger & Norman 1990; Sakamoto et al. 1999a; Knapen et al. 2002; Jogee et al. 2005; Sheth et al. 2005).

NGC 6000 is a nearby ($D \sim 31.6$ Mpc; Pizzella et al. 2005) barred spiral starburst galaxy (star formation rate, SFR $\sim 11 \, M_\odot \, {\rm yr}^{-1}$ based on its $L_{\rm FIR}$; Sanders et al. 2003). Despite its proximity and brightness, this galaxy has not been studied in as great detail as others of similar distance and luminosity, due to its southern declination. *Hubble Space Telescope* observations reveal several bright sources in a circumnuclear star-forming ring or an $m = 1$ nuclear spiral arm and a large-scale ($\gtrsim 1$ kpc) bar (Carollo et al. 1997, 2002; Fathi & Peletier 2003). However, no such barred structures are identified toward the more irregular nuclear region (Carollo 1999; Hunt & Malkan 2004). Infrared observations toward the nucleus of NGC 6000 have found significant polycyclic aromatic hydrocarbon (PAH) emission (Siebenmorgen et al. 2004) and determined a dust temperature of 29.2 ± 2.6 K (Yang & Phillips 2007). NGC 6000 appears bright in CO emission (Young et al. 1995; Mauersberger et al. 1999) as well as H I (Koribalski et al. 2004) as detected

with single-dish telescopes. However, no detailed morphological and kinematical study of the gas content has been performed yet. A compilation of the observed and derived properties for NGC 6000 are presented in Table 1.

In this paper, we present observations of the carbon monoxide emission in the $J = 2$–1 transition of the three brighter isotopologues (^{12}CO, ^{13}CO, C^{18}O) toward NGC 6000 using the Submillimeter Array (SMA; Ho et al. 2004). This is the first high-resolution morphological study of the molecular component toward NGC 6000.

2. OBSERVATIONS

Observations were carried out on 2007 February 20 with the SMA atop Mauna Kea, HI. Seven out of the eight antennas of the array were operational and placed in the "compact-north" configuration, with baselines ranging 16–120 m. The SIS receivers were tuned to the CO $J = 2$–1 frequency (230.538 GHz) in the upper sideband (USB), redshifted to the NGC 6000 average systemic velocity of 2145 km s^{-1} (Albrecht et al. 2007). The correlator was configured so that the $J = 2$–1 transitions of the isotopic substitutions ^{13}CO (220.398 GHz) and C^{18}O (219.560 GHz) were simultaneously observed in the lower sideband (LSB). Spectral resolution was 0.8125 MHz (~ 1 km s^{-1}). System temperatures ranged from 125 to 250 K, with a zenith opacity of 0.1–0.15 as measured at 225 GHz from Caltech Submillimeter Observatory.

A single field (field of view $\sim 55''$ at 230 GHz) was observed toward the central position $\alpha_{J2000.0} = 15^h49^m49^s.40$ and $\delta_{J2000.0} = -29°23'11''.0$ as measured by *IRAS* (Sanders et al. 2003). We achieved a resolution of $2''.8 \times 1''.7$ in the uniform weighted maps and $3''.7 \times 2''.2$ in the natural weighted maps. At the distance of NGC 6000, $1''$ is equivalent to a projected distance of ~ 153 pc. Passband calibration was derived from spectra of Saturn and 3C 279. Absolute flux calibration (within a 10% accuracy) was determined from observations of

Table 1
Summary of Observational Parameters for NGC 6000

Parameter	Value	Reference
Galaxy position		
ROSAT (J2000)	15:49:50.1, −29:23:10.7	1
IRAS (J2000)	15:49:49.4, −29:23:11	2
V_{LSR}	2145 km s^{-1}	3
Distance ($H_0 = 75$ km s^{-1} Mpc^{-1})	31.6 Mpc	4
Morphology		
Morphological type	SB(s)bc	5
Inclination	33°, 27°	6, 7
log D_{25} (0′.1)	1.27	5
Weighted mean luminosity class	4.0	7
Diameter$_{maj \times min}$	2′.3 × 2′.0	8
P.A.	154°, 163°	5, 9
Physical parameters		
T_{dust} (K)	34, 30	10, 11
M_{dust} ($M_\odot$)	1.5×10^9, 2.4×10^7	10, 11
log L_{FIR} ($L_\odot$)	10.83	12
log L_{IR} ($L_\odot$)	10.97	12
log M_{HI} ($M_\odot$)	9.86, 9.8	13, 14
log M_{H2} ($M_\odot$)	8.5	15
log M_{gas} ($M_\odot$)	8.7, 10.0	15, 16
log M_{dyn} ($M_\odot$)	9.8	15

References. (1) Boller et al. 1992; (2) Sanders et al. 2003; (3) Albrecht et al. 2007; (4) Pizzella et al. 2005; (5) de Vaucouleurs et al. 1991; (6) Tully 1988; (7) Corwin et al. 1985; (8) Dressler 1991; (9) Young et al. 1995; (10) Roche & Chandler 1993; (11) Yang & Phillips 2007; (12) Sanders et al. 2003; (13) Martin et al. 1991; (14) Koribalski et al. 2004; (15) This work; (16) Chini et al. 1995.

Callisto. Gain fluctuations were corrected with the nearby quasar J1517−2422 at a distance of 8°.7 from NGC 6000. The applied gain corrections were checked by imaging another nearby quasar, J1625−2527, at a distance of 8°.9. Data calibration and reduction was performed using the MIR-IDL package and imaging using MIRIAD (Sault et al. 1995).

3. RESULTS

3.1. Continuum Emission

Continuum emission from the nucleus of NGC 6000 was imaged using the CO emission free channels in the USB. The spectral energy distribution (SED) of NGC 6000 shows how most of its continuum emission at 1.3 mm stems from thermal dust emission with no significant evidence of free–free contribution (Roche & Chandler 1993). In Figure 1 (left panel), we show the 1.3 mm continuum emission over the average image of the *J*, *H*, and *K* Two Micron All Sky Survey (2MASS) bands (Skrutskie et al. 2006). The position of the peak of emission at $\alpha_{J2000.0} = 15^h49^m49^s.5$, $\delta_{J2000.0} = -29°23'13''$ matches that of 2MASS emission within the resolution. This position also matches within 2″ that of the FIR from low-resolution *IRAS* images (Sanders et al. 2003) and within 1″ that of the Very Large Array 1.4 GHz peak (18″ resolution; Condon et al. 1996). Together with the CO mapping presented in Section 3.2, we have obtained an accurate determination of the nucleus position in NGC 6000, at a just slightly better resolution than the 2″.5 of 2MASS (Skrutskie et al. 2006).

The faint unresolved continuum source has a total flux of 13 ± 3 mJy as measured from our observations. This flux seems to agree with the 18 ± 8 mJy flux observed at 1.3 mm

with the 19″.5 beam of the James Clerk Maxwell telescope (JCMT; Roche & Chandler 1993). However, the JCMT flux might be overestimated given that the contribution of the CO line (Section 3.2) to the continuum in the 64 GHz wide bolometer band would be ∼13 mJy. Therefore, the corrected JCMT continuum flux would be a factor of 2 lower than our measurement. On the other hand, the CO emission would contribute ∼16 mJy to the 42.7 ± 3.9 mJy average flux measured by the 11″ beam of the IRAM 30 m over its 50 GHz bolometer bandwidth (Chini et al. 1995). This corrected flux is a factor of 2 larger than what we recover from our observations. An even larger 1.3 mm flux of 60.6 ± 7.8 mJy was measured by the Swedish-ESO Submillimeter telescope (SEST), which is likely due to its larger beam (24″) collecting most of the extended emission (Chini et al. 1995). Indeed, the extended 1.3 mm continuum emission is estimated to be 98 mJy (CO corrected) in the inner 70″ with the five pointing map observations with the SEST (Albrecht et al. 2007). Assuming the continuum measurements from SEST, we only recovered the compact ∼15% of the continuum emission in our maps.

3.2. Molecular Gas Emission

3.2.1. Comparison to Single Dish

The total integrated flux recovered from the ^{12}CO 2–1 image is 1080 ± 60 Jy km s^{-1}. Single-dish observations of this transition with the 24″ beam of the SEST resulted in a total detected flux of 780 ± 80 Jy km s^{-1} (Chini et al. 1996), where we assumed a conversion factor of ∼25 Jy K^{-1}. This difference is contrary to the expected lower flux in the interferometric maps due to filtering of extended emission. Indeed, the ∼30% flux difference is too large to be attributed to absolute flux calibration error of both SEST and SMA data. Although SEST observations were taken toward a nominal position 2″ away from the position of peak emission derived from our map, this difference would only explain a <4% lower measured flux. In order to understand this measured flux, we convolved our map to a 24″ resolution. The asymmetric lineshape in the data from Chini et al. (1996) clearly differs from that obtained at the center of the convolved map and significantly matches the lineshape at a position ≳5″ south of the central position, consistent with the SEST pointing accuracy. This difference in the observing position easily accounts for a difference in the integrated intensity of >20% with respect to the central position. Though the uncertain comparison with single-dish data does not allow us to accurately determine the missed flux in our maps, we can assume that no significant amount of flux has been filtered out and that most of the extended CO emission has been recovered in our maps.

3.2.2. ^{12}CO Morphology

The total integrated ^{12}CO $J = 2$–1 emission detected in the nuclear region of NGC 6000 is presented in Figure 1 (right panel) on top of the optical *HST* image (Carollo et al. 1997). In addition to the strong nuclear emission, a fainter extended structure is clearly detected (>6σ) extended in the north–south direction, up to a distance of ∼12″ (1.8 kpc) from the center. A similar north–south structure is observed in the near-infrared (Figure 1, left panel).

In Figure 2, we present the maps of the CO $J = 2$–1 integrated emission over the range from 1900 to 2500 km s^{-1} (left panel) and the intensity weighted mean velocities (right panel). The
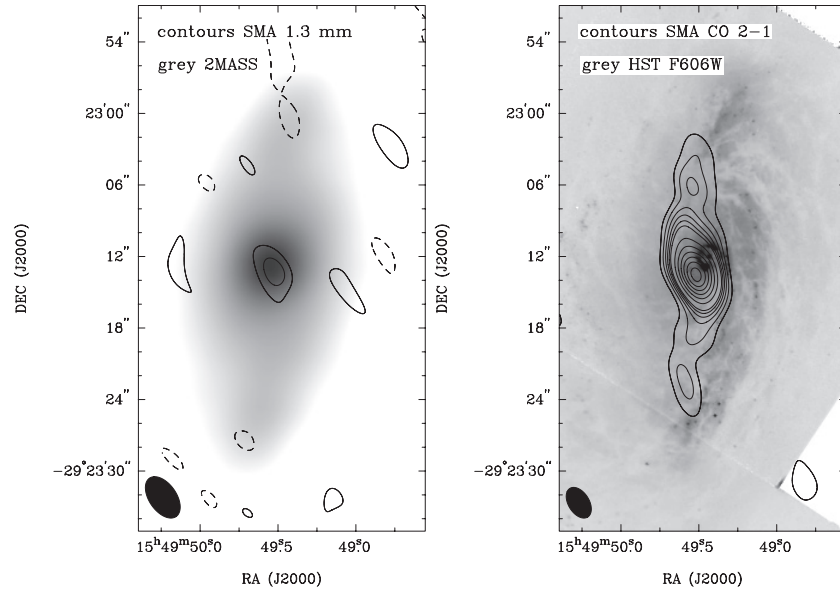
Figure 1. Left panel: 1.3 mm continuum natural weighted emission in NGC 6000 as measured with the SMA (contours) over an average of the *J*, *H*, and *K* 2MASS (gray scale; Skrutskie et al. 2006). Contours levels are 2σ significant as -5, 5, and 10 mJy. 2MASS image is displayed in logarithmic scale. Right panel: composite image of the uniform weighted ^{12}CO $J = 2$–1 integrated emission (contours) and the optical *HST*-WFPC2 image in the F606W filter of NGC 6000 (Carollo et al. 1997). Contours are 3σ levels from 12 to 74 Jy beam^{-1} km s^{-1} and 10σ from 115 to 445 Jy beam^{-1} km s^{-1}, where $\sigma = 4.1$ Jy beam^{-1} km s^{-1} in the image. *HST* image is displayed in logarithmic scale. The respective synthesized beams of each map are displayed in the bottom left-hand corner of each plot.

bright nuclear region is just barely resolved by the $2\rlap{.}''8 \times 1\rlap{.}''7$ (430×260 pc) beam. A Gaussian fit to the UV visibilities in the nuclear emission results in a deconvolved extent of $3\rlap{.}''7 \times 2\rlap{.}''1$ (560×320 pc), centered at $\alpha_{J2000.0} = 15^h49^m49\rlap{.}^s5$, $\delta_{J2000.0} = -29°23'13''$ (see Table 2). The integrated flux from the Gaussian fit to the nuclear region represents an 85% of the total flux recovered in the map (see Section 3.2.1). If we assume that the deconvolved ellipticity is due to the inclination of the circumnuclear molecular disk (Section 4), an inclination of 31° is inferred. This value is in agreement with those derived from large-scale images of NGC 6000. The observed position of the CO emission peak matches the derived dynamical center and is in agreement with that derived from the continuum peak. Similar to what is observed in the near-IR 2MASS images, the peak of CO emission does not coincide with the optical peak of emission due to the strong extinction toward the nuclear region. In fact, the extended CO emission follows the dust lanes seen in the optical.

Optical imaging of the nuclear region of NGC6000 shows a bar-like structure with a nucleus surrounded by an irregular star-forming ring or a $m = 1$ nuclear spiral (Carollo et al. 1997, 2002). Figure 3 shows the redshifted and blueshifted emissions in a close-up view of the central region. The central region of the nuclear spiral, offset by $(\alpha, \delta) \sim (-1'', 1'')$ from the peak of molecular emission, appears to be located at the peak of the high velocity CO emission (Figure 3), right at the eastern edge of the molecular disk. This structure is probably located closer to the observer than the gas disk, and therefore less affected by obscuration. The strongly asymmetrical optical image with respect to the galactic center points to a high extinction, as derived in Section 3.3.2, likely hiding the nuclear and eastern region.

3.2.3. ^{12}CO Kinematics

Figure 4 shows the integrated CO emission over 30 km s^{-1} channels. The resolved molecular emission in the nuclear region is observed over a range of velocities $\Delta v > 400$ km s^{-1} while
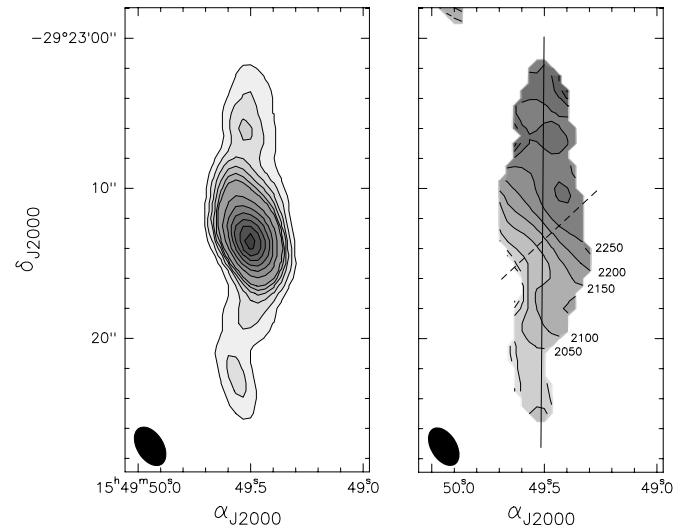
Figure 2. ^{12}CO $J = 2 \rightarrow 1$ integrated emission and kinematics toward the nuclear region of NGC 6000. The synthesized beam of the uniform weighted maps ($2\rlap{.}''8 \times 1\rlap{.}''7$) is plotted at the bottom left-hand corner of each plot. Left panel: integrated flux over the velocity range of 1900 and 2500 km s^{-1}. Contours are similar to those used in Figure 1. Right panel: mean velocity field map. Contours are uniformly spaced by 50 km s^{-1}. Only pixels above 3σ level in integrated intensity map are shown. The solid and dashed lines are the cut directions used for the PV diagrams in Figure 5.

the more extended emission is concentrated in the central $\Delta v \sim 300$ km s^{-1}. As shown in the channel maps (Figure 4), the optical bright structures are located at the regions where the most redshifted emission ($v > 2300$ km s^{-1}) peaks.

We estimated the systemic velocity of NGC 6000 from the Gaussian fit (Table 2) to the profile shown in Figure 7. The fit was performed after masking the asymmetric emission at the highest velocities. The resulting systemic velocity of $V_{LSR} = 2135$ km s^{-1} ($V_{hel} = 2128$ km s^{-1}) is slightly lower than the value of 2145 km s^{-1} derived by Albrecht et al. (2007),

Table 2
Derived Parameters from the CO, ^{13}CO, and C^{18}O Observed Emission

Parameter	CO	^{13}CO	C^{18}O
Gaussian fit to the maps[a]			
Center (J2000.0)	15:49:49.5, −29:23:13	15:49:49.5, −29:23:13	15:49:49.5, −29:23:13
Size (FWHM)	$3\rlap{.}''7 \times 2\rlap{.}''1$, P.A. 12°	$2\rlap{.}''7 \times 2\rlap{.}''1$, P.A. 29°	$2\rlap{.}''5 \times 1\rlap{.}''3$, P.A. 5°
Integrated flux	922 ± 9 Jy km s^{-1}	90 ± 7 Jy km s^{-1}	33 ± 6 Jy km s^{-1}
Central pixel spectra[b]			
V_{LSR}	2135.3 ± 0.3 km s^{-1}	2119 ± 4 km s^{-1}	2104 ± 9 km s^{-1}
$\Delta v_{1/2}$	217.1 ± 0.6 km s^{-1}	196 ± 10 km s^{-1}	150 ± 20 km s^{-1}
T_{B}	5600 mK	400 mK	140 mK

Notes. The conversion factor for the natural weighted maps is 3 K/Jy beam^{-1}.
[a] Results of the deconvolved Gaussian fit models applied to the UV visibilities.
[b] Parameters from the Gaussian fit to the spectra at the central pixel of each map.
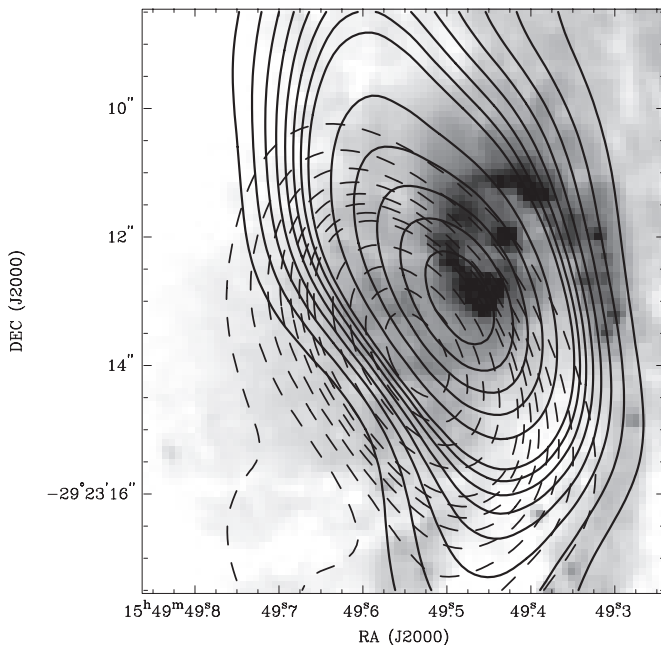
Figure 3. Close-up image of the central region of NGC 6000. The CO redshifted (solid contours) and blueshifted (dashed contours) emissions are plotted over the optical *HST*-WFPC2 image (Carollo et al. 1997). Emission has been integrated −250 and +250 km s^{-1} with respect to the systemic velocity (2135 km s^{-1}) for the blueshifted and redshifted components, respectively. Contours are 3σ levels from 7.5 to 60 Jy km s^{-1} and 10σ from 60 to 185 Jy km s^{-1}, where $\sigma \sim 2.5$ Jy beam^{-1} km s^{-1} in both images. The optical emission is strongly asymmetrical with respect to the dynamical center. We observe that the star-forming ring or the center of the nuclear $m = 1$ spiral (Carollo et al. 1997), significantly offset from the center of the galaxy, is located at the position where the highest velocity CO emission is observed as better seen in the channel maps in Figure 4.

likely due to asymmetry of the profile. However, from the position–velocity (PV) diagrams in Figure 5, it is clear that this systemic velocity is only representing the nuclear molecular component. By measuring the velocity of the extended CO emission in the north–south direction (left panel in Figure 5), we can estimate a systemic velocity for the overall molecular gas of $V_{\mathrm{LSR}} = 2190 \pm 10$ km s^{-1} ($V_{\mathrm{hel}} \sim 2183$ km s^{-1}), in good agreement with the velocity derived from H I observations (Theureau et al. 1998). The difference between both estimates evidences the asymmetry between the molecular gas in the nuclear and the outer regions.

The mean velocity map in Figure 2 (right panel) shows a strong velocity gradient in the central region, with a smoother variation outside the nucleus. The axis of rotation of the central region is oriented in the P.A. = 43° direction. Perpendicular to this axis, the line of nodes, at P.A. = 133°, agrees with previous measurements (see Table 1) and differs from the direction of the bar major axis (P.A. = −25°) derived from elliptical fitting to the isophotal contours of the 2MASS images (Skrutskie et al. 2006). The central velocity gradient is clearly shown by the PV diagrams shown in Figure 5. PV diagrams have been plotted in two different directions: first cut across the whole molecular emission in the north–south direction aimed to include the extended observed features (P.A. = 0°; left panel in Figure 5); second in the line of nodes direction (P.A. = 133°; right panel in Figure 5). Both directions are indicated in the right panel in Figure 2 as continuous and dashed lines, respectively. The PV diagrams in both directions show how in the central 4″ (600 pc) the molecular gas disk is rotating like a rigid-rotor with a rotation velocity $\sim 120 \pm 10$ km s^{-1} per arcsec, equivalent to 0.7 km s^{-1} pc^{-1}, after correcting the velocity for an inclination of $\sim 30°$ (Tully 1988; Corwin et al. 1985). This rotation velocity is similar to the average found in the central regions of the sample of galaxies presented by Sakamoto et al. (1999b) containing barred galaxies like NGC 6000.

3.2.4. ^{13}CO and C^{18}O Emission

The emission of the rarer isotopologues were detected toward the nuclear region. Figure 6 shows the integrated emission of ^{13}CO and C^{18}O compared to that of the main isotopologue. These maps have been natural weighted in order to get a higher sensitivity at the expense of a larger $3\rlap{.}''7 \times 2\rlap{.}''2$ (560 × 340 pc) beam. The nuclear emission is resolved in both ^{13}CO and C^{18}O in the direction of the disk rotation. However, no extended emission in the north–south direction has been detected in the rarer species due to their much lower abundance and lack of enough sensitivity. Still, the two lowest contours plotted for ^{13}CO appear to be slightly elongated in the same direction as the extended emission traced by ^{12}CO. Gaussian models fitted to the visibilities of each isotopologue give the parameters listed in Table 2. We observe the emission of all the three isotopical substitutions to peak at the same position. The spectrum at the central synthesized beam of each of the natural weighted data cubes is shown in Figure 7 in temperature scale. We applied the conversion factor from flux density to synthesized main beam temperature of 3 K/Jy beam^{-1} for these maps. Additionally, the ^{13}CO and C^{18}O spectral features have been multiplied by a factor of 10 for the sake of comparison with the much brighter CO feature.
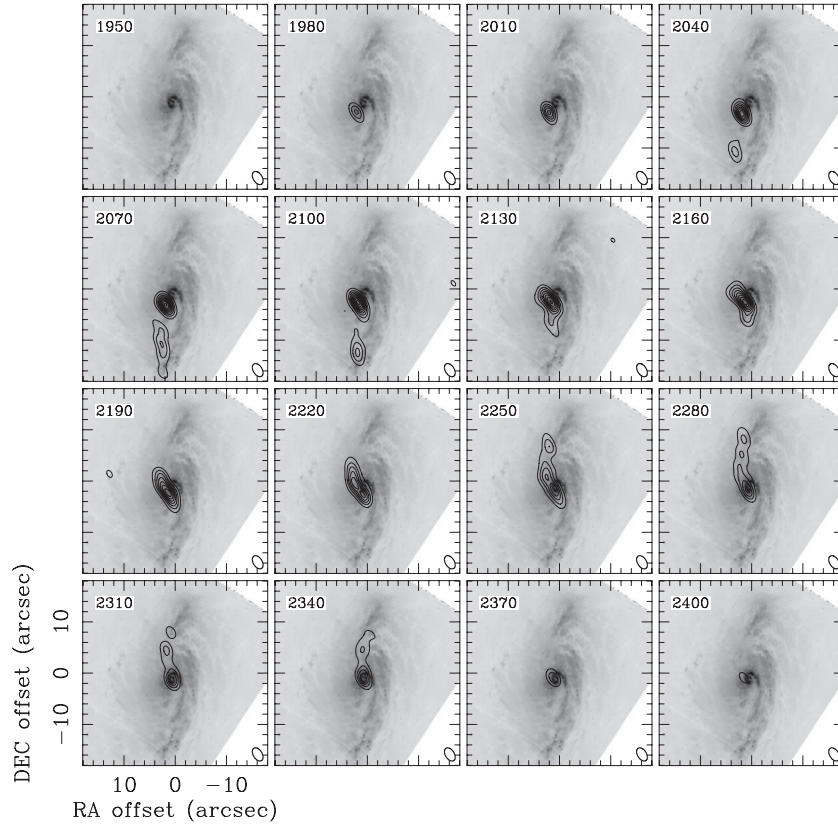
Figure 4. ^{12}CO channel maps (contours) in steps of $30\,\mathrm{km\,s^{-1}}$ plotted over the *HST*-WFPC2 image (Carollo et al. 1997). Contours are plotted at 2σ levels of $1.8\,\mathrm{Jy\,km\,s^{-1}}$. Central velocity of each channel is shown in the upper left corner and beam size in the lower right.
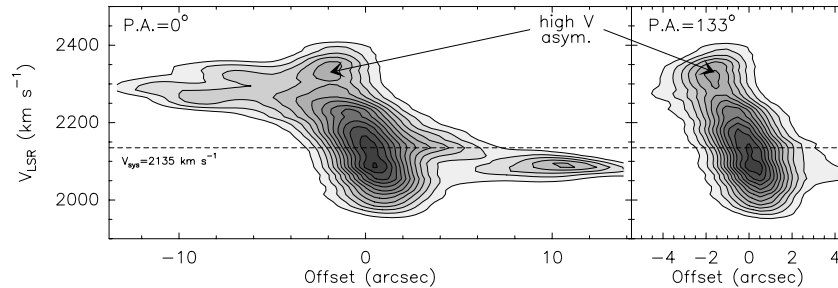
Figure 5. PV diagrams across the nuclear region of NGC 6000 in the P.A. $= 0°$ and P.A. $= 133°$ directions. Contours are 6σ levels (0.15 Jy) from 0.15 Jy to 1.95 Jy. Both cuts directions are shown in Figure 2 by the solid and dashed lines, respectively. The dashed line indicates the systemic velocity. The features corresponding to the high velocity asymmetry observed in the line profiles (Figure 7) and discussed in Section 4.2 are indicated with arrows on both P–V diagrams.

From our observations, we derive an integrated intensity ratio $R^{12/13}_{J=2-1} = I[^{12}\mathrm{CO}_{J=2-1}]/I[^{13}\mathrm{CO}_{J=2-1}]$ of ~ 15.5. Compilation on normal galaxies with $L_{\mathrm{FIR}} < 10^{11}\,L_\odot$ (Taniguchi & Ohyama 1998; Taniguchi et al. 1999) found similar ratios in both CO $J = 1-0$ and $2-1$ of $R^{12/13}_{J=1-0} = 11.3 \pm 3.3$ and $R^{12/13}_{J=2-1} = 12.7 \pm 4.7$. The ratio $R^{16/18}_{J=2-1} \sim 57.9$ calculated with the C^{18}O isotopologue is similar to those derived for other starburst galaxies (Henkel & Mauersberger 1993). Therefore, assuming the isotopic ratios of ^{12}C/^{13}C $= 40$–50 and ^{16}O/^{18}O $= 150$–200 (Henkel & Mauersberger 1993) apply to NGC 6000, we can estimate an opacity of the main isotopologue line of $\tau_{\mathrm{CO}(2-1)} \sim 2.5$–5. Therefore, we can accurately assume both ^{13}CO and C^{18}O to be optically thin. However, this is not the case of the high velocity gas component at $V > 2300\,\mathrm{km\,s^{-1}}$, described in Section 4.2. At the highest velocity range, assuming the same isotopical ratios apply to this region, the measured integrated intensity ratios of $R^{12/13}_{J=2-1} \sim 15$ and $R^{16/18}_{J=2-1} \sim 17$, result in a significant ^{13}CO opacity $\tau_{^{13}\mathrm{CO}(2-1)} \sim 2.5$–4.5 and a lower limits to the large opacity of the main isotope of $\tau_{\mathrm{CO}(2-1)} > 10$.

3.3. Mass Determination

3.3.1. Dynamical Mass

With the derived parameters in Table 2 for central spectra of the CO map, we can make a rough estimate of the total dynamical mass within the nuclear region of NGC 6000. The dynamical mass can be calculated as a function of the disk size and the maximum velocity corrected by inclination as $M_{\mathrm{dyn}} = 250\,M_\odot\,(V_{\mathrm{max}}/\sin(i))^2\,R_{\mathrm{d}}$, where the V_{max} and R_{d} are given in $\mathrm{km\,s^{-1}}$ and pc, respectively. For this calculation, we used the peak velocity of $V_{\mathrm{max}} \sim 180 \pm 20\,\mathrm{km\,s^{-1}}$, with respect to the systemic velocity, reached at a distance of $R_{\mathrm{d}} \sim 1''\!.5 \pm 0''\!.4$
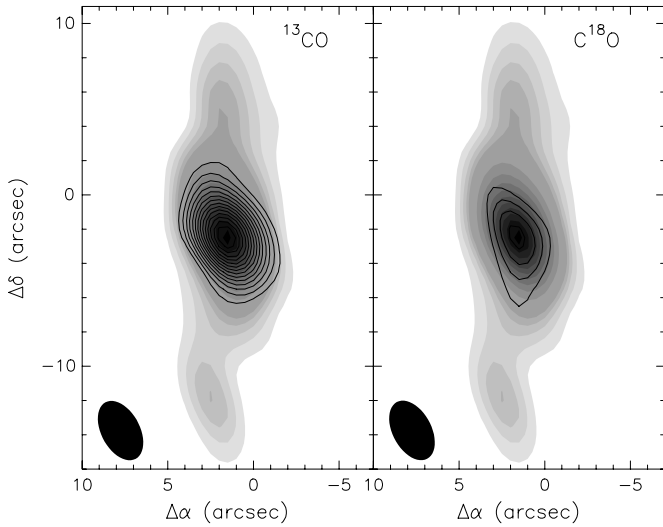
Figure 6. Natural weighted integrated flux maps of the observed $J = 2 \rightarrow 1$ transition in the different CO isotopologues (contours), compared to the ^{12}CO emission (gray scale). The beam size in these maps is $3''\!.7 \times 2''\!.2$ (shown as filled ellipses at the bottom left corner). ^{12}CO gray scale levels correspond to those in Figure 2. Contours are 2σ levels (4.4 Jy beam^{-1} km s^{-1}) in both ^{13}CO and C^{18}O.

Figure 7. Brightness temperature spectra of the three isotopologues extracted from the central synthesized beam of the natural weighted data cubes. The resolution in velocity is of 10 km s^{-1} for the main isotope, 20 km s^{-1} for ^{13}CO, and 30 km s^{-1} for C^{18}O. The spectra of ^{13}CO and C^{18}O have been multiplied by a factor of 10 for the sake of clarity in the comparison. The dashed line indicates the systemic velocity $V_{\rm sys} = 2135$ km s^{-1} determined from the Gaussian fit to the CO profile. We indicate the high velocity asymmetry observed to the overall Gaussian profile. See the text in Section 4.2 for a discussion on this feature.

as measured in the southeast direction of the molecular disk (low velocity end in Figure 5) so that we avoid the uncertainty due to the disk asymmetry at the higher velocities (Section 4). This approximation yields a total mass $M_{\rm dyn} = 7^{+5}_{-3} \times 10^9\, M_\odot$.

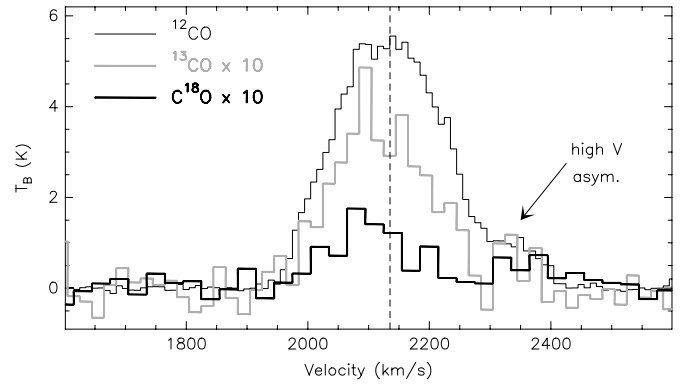### 3.3.2. Mass of Molecular Gas Traced by CO

In order to get an accurate estimate of the mass of molecular hydrogen traced by the carbon monoxide, we will use the total flux detected of the isotopologue C^{18}O emission. This is equivalent to using the main isotopologue corrected by opacity effects. Assuming optically thin emission and LTE conditions, we can get the mass of hydrogen as

$$N_{\rm H_2} = (7 \pm 2) \times 10^{18}\, \frac{[^{12}\rm C^{16}O]}{[^x\rm C^yO]} \int T_{\rm b}^{^x\rm C^yO_{J=2-1}}\, dv \; \rm cm^{-2}, \quad (1)$$

where ^{12}C^{16}O/^{x}C^{y}O is the ratio between the main form of carbon monoxide and any given isotopologue. This expression can be applied for the three isotopologues and assumes a CO fractional abundance ^{12}CO/H$_2 \sim 8.5 \times 10^{-5}$ (Frerking et al. 1982) and $T_{\rm ex} = 30 \pm 10$ K, similar to the dust temperature derived by Yang & Phillips (2007). Under these conditions and with a constant factor of $(1.9 \pm 0.6) \times 10^{19}$ calculated for the $J = 1$–0 transition, Equation (1) is equivalent to Equation (3) in Paglione et al. (2001). With the total flux observed in C^{18}O and the ratio ^{16}O/^{18}O$\sim$150 (Harrison et al. 1999), we derive an average $N_{\rm H_2} = (1.0 \pm 0.3) \times 10^{23}$ cm^{-2}. This amount of molecular hydrogen implies a visual extinction of $A_v \sim 100$ mag toward the central region of NGC 6000 which is certainly responsible for the asymmetric optical structure of the nucleus of NGC 6000.

We estimate a total mass of molecular gas in the nuclear region of $M_{\rm H2} \sim 2.9 \pm 0.9 \times 10^8\, M_\odot$ within the central projected $\sim$566 × 321 pc (as measured from the deconvolved CO source size).

From the CO map in Figure 1, we estimate that $\sim$85% of the molecular mass in NGC 6000 is concentrated in the nuclear $\sim$3$''$ region ($\sim$460 pc). This percentage is just a lower limit given the significant opacity affecting the CO emission mostly toward the

central peak of emission. Therefore, we can estimate a total mass of molecular gas of $3.5 \times 10^8\, M_\odot$ within the inner $\sim$1.8 kpc. Assuming a correction factor 1.36 for the He and heavier elements (Allen 1973), we can estimate a total mass of gas $M_{\rm gas} = 4.6 \times 10^8\, M_\odot$, which yields a ratio $M_{\rm gas}/M_{\rm dyn} \sim 6\%$.

4. DISCUSSION

4.1. Bar-driven Molecular Gas Fueling the Starburst in NGC 6000

The study of the molecular gas content in a sample of 20 galaxies by Sakamoto et al. (1999a) statistically shows that the gas tends to be more concentrated in the central kiloparsec in barred systems. This is the case of NGC 6000 where most of the gas is located in the inner half kiloparsec (Section 3.3.2). The large-scale bar revealed in the NIR may also have a fingerprint in the molecular gas kinematics described in this work. We observe that the P.A. = 0° PV diagram in Figure 5 (right panel) shows how the extended molecular component displays a S-shaped feature. This kinematic signature can be understood as the non-circular motions in the context of a barred potential (Binney et al. 1991). The inner material could be moving in the barely resolved x_2 orbits which, with the resolution of our maps, would look like a molecular disk. On the other hand, the external gas would be moving in large elliptical x_1 orbits traced as the S-shaped profile in the PV diagram. Indeed, the north–south extended emission could be understood as the molecular material infalling from the x_1 toward the x_2 orbits as observed in simulations of the nuclear spiral region simulations ($r < 2$ kpc; Athanassoula & Bureau 1999). Similar signatures of a barred potential are observed in the PV diagrams of other galaxies such as NGC 1530 and NGC 4258 (Downes et al. 1996; Cox & Downes 1996), and equivalent structures are found in their innermost regions. Higher resolution imaging of NGC 6000 might support the scenario of a barred potential by resolving the inner disk structure into circular x_2 orbits as observed by Meier et al. (2008) toward Maffei 2 and by revealing the fine kinematic signatures expected from models (Athanassoula & Bureau 1999).

However, our measured $M_{\rm gas}/M_{\rm dyn}$ ratio of 6% is lower than the average measured by Sakamoto et al. (1999a) in starbursts

and barred galaxies. This measurement is significantly affected by the way the gas mass is calculated. Indeed, adopting their same conversion factor ($X_{CO} = 3 \times 10^{20}$ cm^{-2}(K km s^{-1})$^{-1}$ rather than $X_{CO} = 0.4 \times 10^{20}$ cm^{-2}(K km s^{-1})$^{-1}$, see Section 4.3), the measured ratio would increase up to ~35%. This ratio is only found in barred starbursts in the Sakamoto et al. (1999a) sample.

4.2. The High Velocity Asymmetry

The strong asymmetry in the nuclear ring/disk is also a particularly interesting feature. As seen in Figure 5, a significant part of the molecular gas traced by CO is skewed toward the region at the lowest velocities, corresponding to the southeast disk component. However, the emission at the highest velocities from 2300 to 2400 km s^{-1} in the PV diagrams, although following the same rotation gradient, seems to be significantly detached from the inner rotating structure. This feature at the highest velocities corresponds to the wing observed in the spectrum shown in Figure 7. We discard the possibility of self-absorption at high velocities, which would change the systemic velocity derived from the Gaussian fit to the line, as the optically thin ^{13}CO and C^{18}O show similar profiles and are centered at the same velocity. It is surprising that ^{13}CO and even C^{18}O are detected in this velocity component between 2300 and 2400 km s^{-1}. As derived in Section 3.2.4, the low ratio of ^{13}CO and C^{18}O with respect to the main isotopologue implies that a significant opacity is affecting even the ^{13}CO emission in this molecular component. CO being optically thick can provide some constraint on the extent of the emission as compared to our resolution. From the CO brightness temperature measured $T_b \sim 1$ K and assuming an excitation temperature $T_{ex} = 30$ K (as derived from the dust temperature, Yang & Phillips 2007, and assuming CO being thermalized at this temperature), we estimate the region extent to be <80 pc (<0''.5). This is slightly above the ~50 pc typical size of giant molecular clouds within our Galaxy. This giant molecular cloud within the inner region of NGC 6000 must be very dense and more compact than our estimate to explain such CO opacity. It could have originated as a shock between the circumnuclear disk and the infalling molecular gas along the dust lanes. Moreover, emission arises from the same location as the center of the nuclear spiral observed in the optical (Carollo et al. 1997; Figure 3), which suggest that this dense and compact molecular cloud might be directly related to the fueling of star formation event in this region.

4.3. CO-to-H$_2$ Conversion Factor in Starburst Galaxies

We can estimate the column density of molecular gas via the conversion factor $X_{CO} = N(H_2)/CO = 3.0 \times 10^{20}$ cm^{-2}(K km s^{-1})$^{-1}$ based on measurements of galactic disk molecular clouds (Solomon et al. 1987). This way, and adopting the CO integrated intensity in this work, we derive a H$_2$ column density of 7.5×10^{23} cm^{-2} which is almost an order of magnitude larger than the value derived from the optically thin C^{18}O line (Section 3.3.2). As already observed toward the starburst NGC 253 (Mauersberger et al. 1996; Harrison et al. 1999), the conversion factor in the starburst environment might be significantly lower than that in the Galactic disk. From our measurements, we calculate a conversion factor $X_{CO} = 0.4 \times 10^{20}$ cm^{-2}(K km s^{-1})$^{-1}$ in agreement with that derived for NGC 253 (Mauersberger et al. 1996). This result supports the evidences found for a lower conversion factor in

the central region of galaxies, and in particular in starbursts with respect to the Galactic disk (Downes & Solomon 1998).

We note that conversion factors usually refer to CO $J = 1$–0 instead of the $J = 2$–1 we use in our work. The ratio between both lines is $2 - 1/1 - 0 \sim 1.46$ as observed by Chini et al. (1996). Assuming this ratio directly implies a similar increase to the $X_{CO(1-0)}$ conversion factor, it would result in a factor $X_{CO} \sim 0.6 \times 10^{20}$ cm^{-2}(K km s^{-1})$^{-1}$. Nevertheless, this conversion is still a factor of 5 below that in the Galactic disk.

5. SUMMARY

We have obtained high-resolution ($2''.8 \times 1''.7$) maps of the molecular emission toward NGC 6000 as traced by the $J = 2$–1 transition of carbon monoxide with the SMA. Emission from the three main isotopologues of carbon monoxide, ^{12}CO, ^{13}CO, and C^{18}O are detected. Both the continuum and molecular emission peak at the same position. From these measurements, we have accurately determined the nucleus position in NGC 6000 at $\alpha_{J2000.0} = 15^h49^m49^s.5$ and $\delta_{J2000.0} = -29°23'13$, in agreement with previous IR determinations. More than an 85% of the emission is concentrated toward the nuclear projected ~400 × 300 pc region, where we estimate optical extinctions of the order of ~100 mag. Such large obscuration is likely responsible for the asymmetry in the optical images, probably hiding the eastern part of the nuclear region at these wavelengths.

The emission from the central region is resolved in the direction of the observed velocity gradient. Molecular emission is detected in the north–south direction extended up to distances of >1.5 kpc from the center. However, this is only detected in the main isotopologue. Both the nuclear and extended emissions show dynamical evidences that might be explained by the presence of a bar potential affecting the molecular material, likely responsible of the strong nuclear concentration and maybe the starburst event. We observed a high velocity component which appears to be detached from the nuclear disk/ring and is highly optically thick. With an estimated extent of <80 pc, this giant molecular cloud is likely to be related to the fueling of the nuclear star burst in NGC 6000.

The ratios of ^{13}CO and C^{18}O with respect to the main isotopologue are similar to the average measured in similar starburst galaxies with luminosities $L_{FIR} < 10^{11} L_{\odot}$ in the literature (Henkel & Mauersberger 1993).

The total dynamical mass derived for NGC 6000 is $1.9 \times 10^9 M_{\odot}$. We estimate a total mass of molecular gas of $4.6 \times 10^8 M_{\odot}$ and a ratio $M_{gas}/M_{dyn} \sim 6\%$, similar to the starbursts in the barred galaxy sample by Sakamoto et al. (1999a). The independent estimate of the molecular mass with the optically thin C^{18}O isotope allows the determination of the conversion factor CO-to-H2 of $X_{CO} = 0.4 \times 10^{20}$ cm^{-2}(K km s^{-1})$^{-1}$, which agrees with previous estimates that measure a lower factor in starburst nuclear regions (Mauersberger et al. 1996) as compared with the standard factor derived for Galactic disk clouds.

REFERENCES

Albrecht, M., Krügel, E., & Chini, R. 2007, A&A, 462, 575
Allen, C. W. (ed.) 1973, Astrophysical Quantities (London: Athlone Press)
Athanassoula, E., & Bureau, M. 1999, ApJ, 522, 699
Binney, J., Gerhard, O. E., Stark, A. A., Bally, J., & Uchida, K. I. 1991, MNRAS, 252, 210
Boller, T., Meurs, E. J. A., Brinkmann, W., Fink, H., Zimmermann, U., & Adorf, H.-M. 1992, A&A, 261, 57
Carollo, C. M. 1999, ApJ, 523, 566
Carollo, C. M., Stiavelli, M., de Zeeuw, P. T., & Mack, J. 1997, AJ, 114, 2366
Carollo, C. M., Stiavelli, M., Seigar, M., de Zeeuw, P. T., & Dejonghe, H. 2002, AJ, 123, 159
Chini, R., Kruegel, E., & Lemke, R. 1996, A&AS, 118, 47
Chini, R., Kruegel, E., Lemke, R., & Ward-Thompson, D. 1995, A&A, 295, 317
Condon, J. J., Helou, G., Sanders, D. B., & Soifer, B. T. 1996, ApJS, 103, 81
Corwin, H. G., de Vaucouleurs, A., & de Vaucouleurs, G. 1985, Univ. Texas Monogr. Astron., 4, 1
Cox, P., & Downes, D. 1996, ApJ, 473, 219
de Vaucouleurs, G., de Vaucouleurs, A., Corwin, H. G., Jr., Buta, R. J., Paturel, G., & Fouque, P. 1991, Third Reference Catalogue of Bright Galaxies, Vols. 1–3 (Berlin: Springer), 2069
Downes, D., Reynaud, D., Solomon, P. M., & Radford, S. J. E. 1996, ApJ, 461, 186
Downes, D., & Solomon, P. M. 1998, ApJ, 507, 615
Dressler, A. 1991, ApJS, 75, 241
Fathi, K., & Peletier, R. F. 2003, A&A, 407, 61
Frerking, M. A., Langer, W. D., & Wilson, R. W. 1982, ApJ, 262, 590
Harrison, A., Henkel, C., & Russell, A. 1999, MNRAS, 303, 157
Henkel, C., & Mauersberger, R. 1993, A&A, 274, 730
Ho, P. T. P., Moran, J. M., & Lo, K. Y. 2004, ApJ, 616, L1
Hunt, L. K., & Malkan, M. A. 2004, ApJ, 616, 707
Jogee, S., Scoville, N., & Kenney, J. D. P. 2005, ApJ, 630, 837
Knapen, J. H., Pérez-Ramírez, D., & Laine, S. 2002, MNRAS, 337, 808
Koribalski, B. S., et al. 2004, AJ, 128, 16
Martin, J. M., Bottinelli, L., Gouguenheim, L., & Dennefeld, M. 1991, A&A, 245, 393
Mauersberger, R., Henkel, C., Walsh, W., & Schulz, A. 1999, A&A, 341, 256
Mauersberger, R., Henkel, C., Wielebinski, R., Wiklind, T., & Reuter, H.-P. 1996, A&A, 305, 421
Meier, D. S., Turner, J. L., & Hurt, R. L. 2008, ApJ, 675, 281
Paglione, T. A. D., et al. 2001, ApJS, 135, 183
Pérez-Ramírez, D., Knapen, J. H., Peletier, R. F., Laine, S., Doyon, R., & Nadeau, D. 2000, MNRAS, 317, 234
Pfenniger, D., & Norman, C. 1990, ApJ, 363, 391
Pizzella, A., Corsini, E. M., Dalla Bontà, E., Sarzi, M., Coccato, L., & Bertola, F. 2005, ApJ, 631, 785
Roche, P. F., & Chandler, C. J. 1993, MNRAS, 265, 486
Sakamoto, K., Okumura, S. K., Ishizuki, S., & Scoville, N. Z. 1999a, ApJ, 525, 691
Sakamoto, K., Okumura, S. K., Ishizuki, S., & Scoville, N. Z. 1999b, ApJS, 124, 403
Sanders, D. B., Mazzarella, J. M., Kim, D.-C., Surace, J. A., & Soifer, B. T. 2003, AJ, 126, 1607
Sault, R. J., Teuben, P. J., & Wright, M. C. H. 1995, in ASP Conf. Ser. 77 Astronomical Data Analysis Software and Systems IV, ed. R. A. Shaw, H. E. Payne, & J. J. E. Hayes (San Francisco, CA: ASP), 433
Sheth, K., Vogel, S. N., Regan, M. W., Thornley, M. D., & Teuben, P. J. 2005, ApJ, 632, 217
Siebenmorgen, R., Krügel, E., & Spoon, H. W. W. 2004, A&A, 414, 123
Skrutskie, M. F., et al. 2006, AJ, 131, 1163
Solomon, P. M., Rivolo, A. R., Barrett, J., & Yahil, A. 1987, ApJ, 319, 730
Taniguchi, Y., & Ohyama, Y. 1998, ApJ, 507, L121
Taniguchi, Y., Ohyama, Y., & Sanders, D. B. 1999, ApJ, 522, 214
Theureau, G., Bottinelli, L., Coudreau-Durand, N., Gouguenheim, L., Hallet, N., Loulergue, M., Paturel, G., & Teerikorpi, P. 1998, A&AS, 130, 333
Tully, R. B. 1988, Nearby Galaxies Catalog (Cambridge: Cambridge Univ. Press), 221
Yang, M., & Phillips, T. 2007, ApJ, 662, 284
Young, J. S., et al. 1995, ApJS, 98, 219